Int J Adv Manuf Technol (2017) 92:1299–1314
DOI 10.1007/s00170-017-0213-5

ORIGINAL ARTICLE

Flow analysis of the laminated manufacturing system with laser sintering of metal powder. Part I: flow uniformity inside the working chamber

Wei-Cheng Wang[1] · **Chia-Yao Chang**[1]

Received: 14 December 2016 / Accepted: 22 February 2017 / Published online: 10 March 2017
© Springer-Verlag London 2017

Abstract Selective laser melting (SLM) as a part of 3D printing technology has been a novel industrial manufacturing process nowadays. However, the collection of metal powders emitted from the working plane is significant for the SLM process. The uniformity of the flow passing through the SLM working chamber, which helps collect emitted powders, has been considered as a key solution. In this study, for the purpose of improving the flow uniformity, a blow-to-suction device composed of a trapezoid push nozzle, a working chamber, and a suction tunnel was applied. Various parameters, such as the width of trapezoid push nozzle, the width of suction tunnel, and the nozzle-to-plane distances, were examined experimentally and computationally. Hot-wire velocity measurement and smoke flow visualization were used to verify the reliability of the simulation. Through the results of degree of uniformity (DOU), the momentum exchange between the suction and blow sides plays an important role for producing a uniform flow through the working chamber. In addition, higher suction velocity as well as larger nozzle-to-plane distance result in relatively better uniformity of the flow.

Keywords Selective laser melting · 3D printing · Flow uniformity · Experimental fluid dynamics · Computational fluid dynamics · Flow visualization

✉ Wei-Cheng Wang
wilsonwang@mail.ncku.edu.tw

[1] Department of Aeronautics and Astronautics, National Cheng Kung University, Tainan, Taiwan 70101

1 Introduction

Based on the rapid prototyping, the 3D printing technology, which can be classified into many types owing to the different laminated manufacturing and materials used in processing, is widely applied to the industrial design and manufacturing nowadays. In order to overcome the limitations of the traditional product such as material deformation molding and cutting machining processing, a selective laser melting (SLM) technology with a high energy laser beam fuses the metal powder into liquid and produces metal products with a high mechanical strength and consistency. It greatly increases the range of applications and applicability of the 3D printing products.

Many difficulties have been raised for SLM technology in the laminated manufacturing system, and among these, metal powder ejection is considered to be the most significant one. Metal powders eject randomly and absorb or scatter partial laser energy during the SLM process [1]. It severely affects the quality of the end products. The more uniform carrier gas flow through the working plane, the higher stability of the lamination, and the better porosity of the internal structure will be. Dai and Gu [2] found a dramatic difference in the quality of the end product when conducting the SLM process with various linear energy densities (LEDs) due to the change in flow field at the center of the working plane. The results showed that creating a uniform flow structure to successfully remove the ejected metal particles plays a significant role in the SLM process. To maintain the quality of the SLM process, a better flow control inside the chamber of laminated manufacturing system has to be carried out.

Similar to the chamber of the SLM system, a so-called push-pull flow system has been investigated intensively, for the purpose of improving the pollutant removal from the system [3–14]. The flow behaviors and structures were studied

using flow measurement and flow visualization techniques. Marzal et al. [3–6] conducted a series of researches for the development of an analytical model determined through the push nozzle geometry and interpreted the capture efficiency of the surface treatment tank for reducing the pollutants coming from a fume hood. As shown in Fig. 1, the flow mechanisms in the push-pull ventilation system were identified into four areas: (1) the feedback current under semi-free jets, (2) the curtain impacts on the tank which produce a strong distortion, (3) the reorganized flow as it flows over the surface, and (4) the current entering the bottom of the exhaust hood. The flow visualization results show the correlation between the field characteristics and the containment leakage levels of the conventional range hood. The complicated flow patterns were induced around the bottom edge of the sash when the environmental air was sucked into the hood. Tseng et al. [7] investigated the boundary layer separation and flow recirculation around the fume hood's doorsill. The results showed that the side posts are the primary sources of the non-uniform flow, which contributes the contaminant leakage. Huang et al. [7–14, 16] thereafter developed a new type of push-pull ventilation system, known as an air-curtain fume hood using a push-pull air curtain technique. The push jet and suction flow were designed to create a push-pull air curtain in the sash plane for aerodynamically separating the interior of the cabinet from the outside atmosphere. They also observed the gas transport process through the laser-light sheet scattering flow visualization method assisted with the smoke particles. The aerodynamic characteristics are classified into dispersion, transition, encapsulation, and strong suction. Dai and Gu [2] revealed the gaseous bubble movement in the melt pool for the increasing LEDs. For a relative low LED, most of the bubbles are entrapped below the surface of the melt pool due to the lower speed obtained by the bubbles. As the LED increased to 17.5 kJ/m, a majority of bubbles escaped from the melt pool easily at high movement speeds. The gas removal efficiency was enhanced, and the maximum relative density of laser powders reached 96%. As the applied LED was higher than 20 kJ/m, the Marangoni flow tended to remain the entrapped gas bubbles and the flow pattern has a tendency to deposit the gas bubbles at the melt bottom or to agglomerate gas bubbles by the rotating flow in the melt pool. As LED further increased to 22.5 kJ/m, the gaseous bubbles were entrapped and moved easily by larger-scale vortex and the bubbles were transported to the center of the rotating flow due to the lower density of the gas and the melt multiphase mixture. To sum up, reducing turbulent dispersions induced by boundary layer separation and flow recirculation are the key point to create a uniform air curtain in the SLM chamber and eventually ensure the quality of the process and the products.

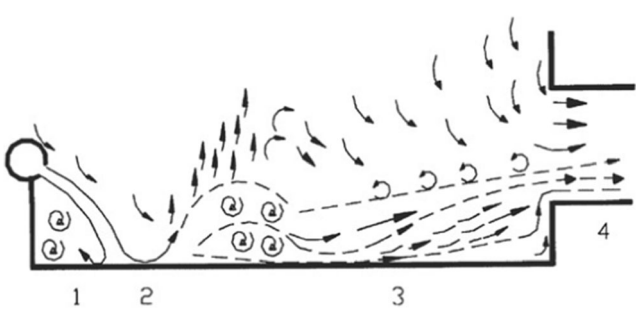

Fig. 1 Types of flow in a push-pull ventilation system applied to surface treatment tank

The objectives of this study is to analyze and control the flow field in the SLM chamber of the laminated manufacturing system, for the purpose of capturing all the metal powders in a blow-to-suction device. We conducted numerical simulations across the chamber as well as verified the simulation results experimentally using flow measurement and flow visualization on a 1:1 lab-scale model.

2 Experimental method

2.1 Experimental setup

The experiment was conducted in a blow-to-suction working chamber, which consists of a trapezoid push nozzle, a cuboid chamber, and a suction device. As shown in Fig. 2, it was built to simulate the industrial 250 mm × 250 mm SLM chamber. The experimental working chamber was made of acrylic and assembled by the aluminum extrusion tooling. The transverse length and width in z and x directions are 605 and 325 mm, respectively. The height of the working plane can be adjusted between 414 and 464 mm using a pressure-regulating valve with no leakage.

The trapezoid push nozzle was designed to have five vertical plates properly arranged and one flow field development area to reduce the turbulence intensity and increase the flow uniformity.

The suction device was designed as a tunnel with four curvy vertical plates, for the purpose of arranging the suction flow. The widths of push nozzle and suction tunnel vary from 20 to 50 mm. The nozzle-to-plane distances, which are defined as the distance from the bottom of the push nozzle or the suction tunnel to the working plane, varied in the range of 20~80 mm.

Figure 3 shows the experimental layout applied in this study. Both blow and suction airflows were driven by the 2hp turbo-fan air blowers, controlled by the frequency converters to adjust the blow and suction flow speeds. Two Venturi flow meters were installed respectively at the inlet and outlet pipelines to control the flow rates. The push-nozzle velocity (V_b), defined as the area with average blowing velocity at the exit of the push nozzle, as well as the suction flow velocity (V_p), defined as the area with average suction

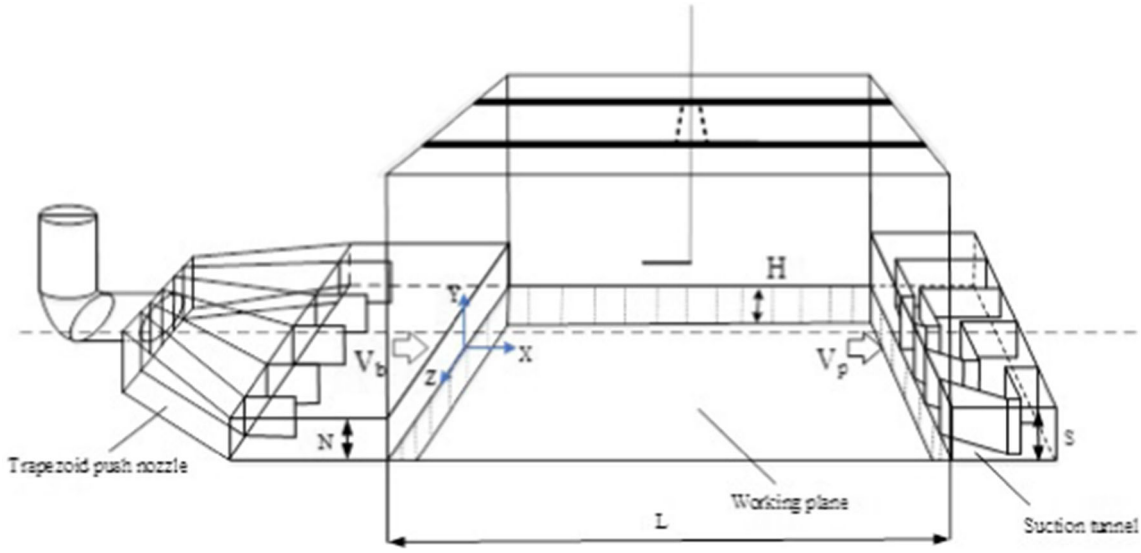

Fig. 2 Definitions of geometric parameters

velocity at the opening of the suction side, were adjusted within the range of 0–7 and 0–10 m/s, respectively, by controlling the air blowers and flow meters.

The blow and suction velocities, the nozzle-to-plane distances, and widths of the push nozzle/suction tunnel are the primary factors that influence the flow characteristics of the SLM chamber.

2.2 Velocity measurement

The velocity measurement inside the chamber was carried out by a constant-temperature, cross-type hot-wire probe, made of a platinum wire with 5 mm diameter. Two DISA55M01 constant-temperature anemometers are connected with the hot-wire probe for measuring the streamwise (X) and

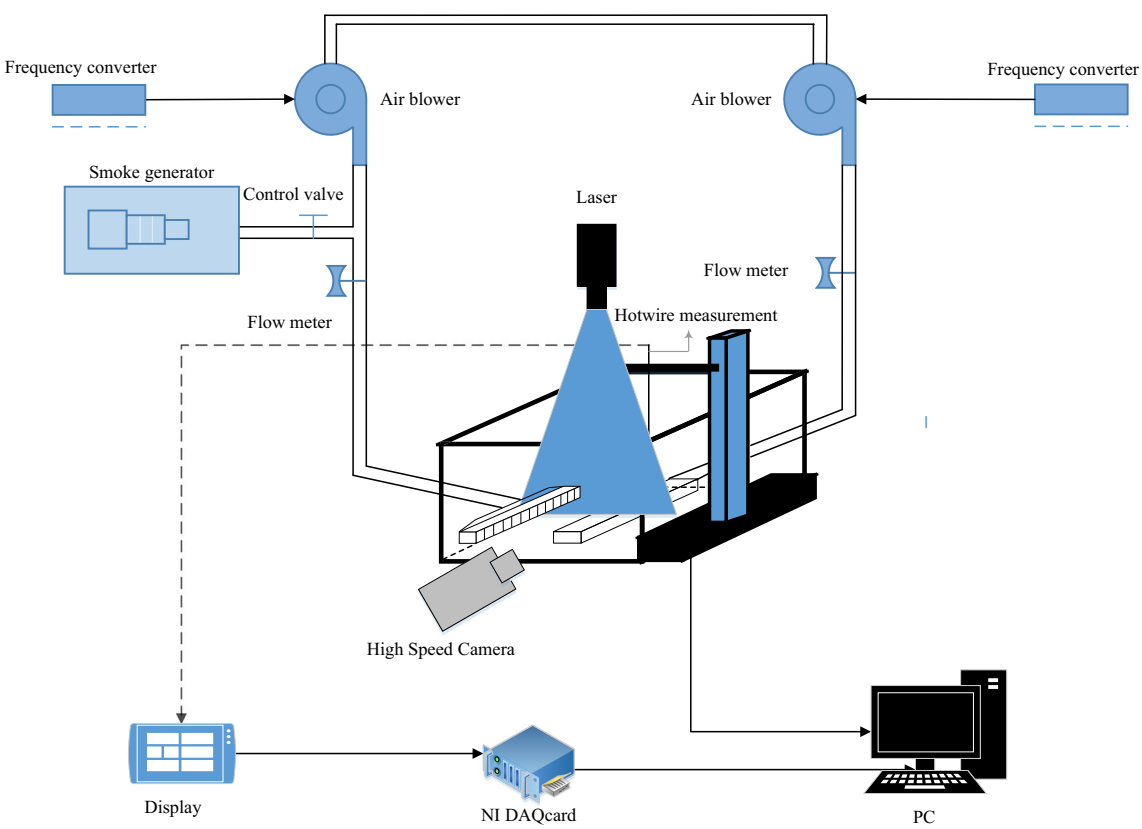

Fig. 3 Experimental setup

transverse (*Y*) velocity components of the flow. The frequency response of the hot wire is about 30 kHz and is detected through a PCI-6123 analog/digital converter with BNC-2110 connector.

A two-axis traversing mechanism, which is driven by two STP-4 step motors, is also connected with the hot-wire anemometer to control the path. The hot-wire anemometer was calibrated every 3 h to avoid the influences of the air temperature variation, the small particle deposition, and the wire oxidation. The calibration was conducted using a low-speed, open-jet wind tunnel and a pitot-static tube at the flow speeds of 5 to 25 m/s. The nozzle outside the wind tunnel has dimensions of 12 mm (*H*) × 300 mm (*W*) and an aspect ratio of 25. The turbulence intensity of the wind tunnel at the nozzle exit center is below 0.5%. A pitot-static tube installed at the nozzle exit of the calibrating wind tunnel is connected to a pressure transducer (model CD 23, Validyne Engineering Corp., California, USA) with the maximum measurable pressure of 0.55 kPa and the accuracy of 0.25%. It was pre-calibrated by a micro-manometer with the accuracy of ±0.005 mmH_2O.

The 512 A/D converter of IQ-Tech 16-bit resolution data acquisition card was used for acquiring the experimental data. The value of maximum sampling frequency is 10 kHz, and the operating voltage range is in-between 5 V.

2.3 Flow visualization

Smoke visualization was applied to confirm the flow patterns and flow structures inside the working chamber using the Mie scattering technique with a strong and stable lighting source. The diode-pumped solid-state (DPSS) laser (MGL-F-532-2W, Unice E-O Services, Inc., Taoyuan, Taiwan) with a cylindrical

Table 1 Computational parameters for simulating the working chamber

Problem type	Flow turbulence
Turbulence model	Standard k-epsilon
Wall function	Standard wall
Fluid	N_2
Density (kg/m^3)	1.1614
Viscosity (kg/m·s)	1.846×10^{-5}
Pressure (Pa)	101,300
Inlet boundary type	Velocity inlet
Velocity inlet (m/s)	7
Inlet turbulence intensity for kinetic energy	0.045
Hydraulic diameter for dissipation rate (m)	0.05
Outlet boundary type	Pressure outlet
Grids	2,625,713
Gravity in *Y*-direction (m/s^2)	−9.81
Initial *X*-direction velocity (m/s)	1*E*−006
Initial *Y*-direction velocity (m/s)	1*E*−006
Initial *Z*-direction velocity (m/s)	1*E*−006
Linear solver	AMG
Residual error	1×10^{-4}
Max. iterations	2000
Min. residual	1*E*−018
Spatial differencing method	
Velocity	2nd order
Turbulence	2nd order
Solvers sweeps	500
Inertial relaxation	0.2
Linear relaxation	0.1
Turbulence viscosity ratio	65

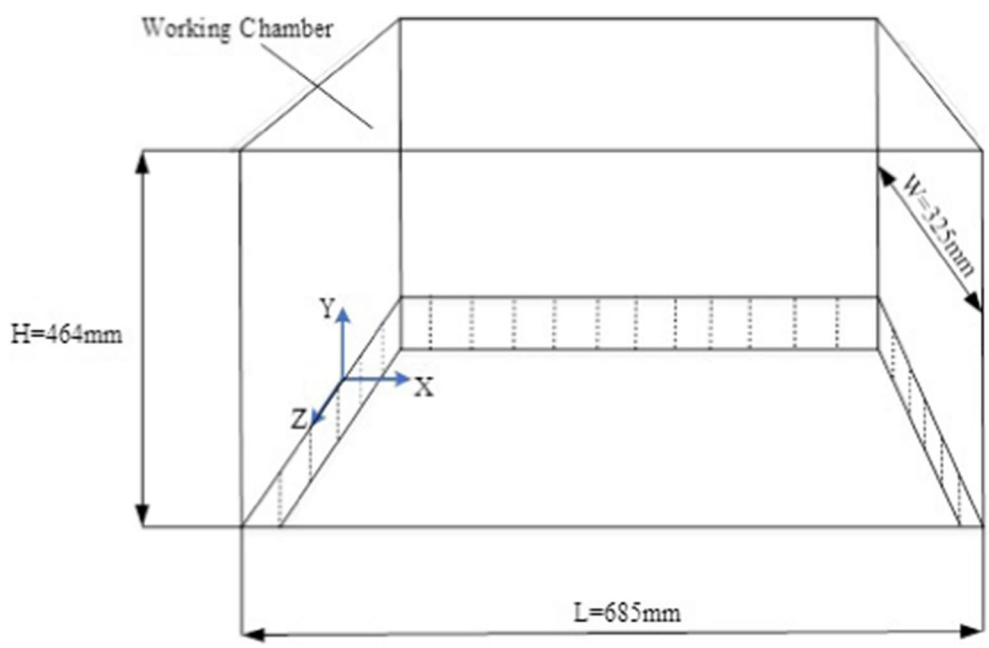

Fig. 4 The geometry of the working chamber

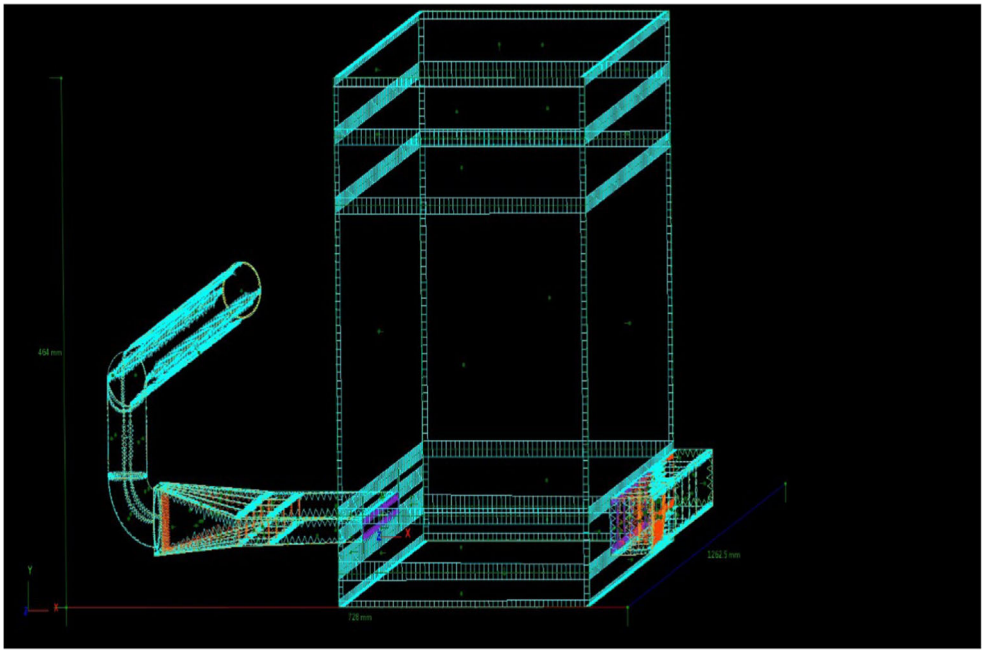

Fig. 5 The Mesh geometry system

lens was used to create the laser sheet for different sectional flow fields. Smoke was generated by the smoke generator (Z-800IIR, Antari Fog Machine, Taoyuan, Taiwan) fed with mineral oil and operated in 0.7 kW power consumption. The flow behavior can be easily observed when the smoke passed through the tube and the trapezoid push nozzle. The images of flow visualization were recorded by IDT Vision N4 series high-speed cameras, and the resolution of the all-axes charge-coupled device (CCD) can be up to 2336 × 1728. It could record the maximum 5000 frames per second (fps).

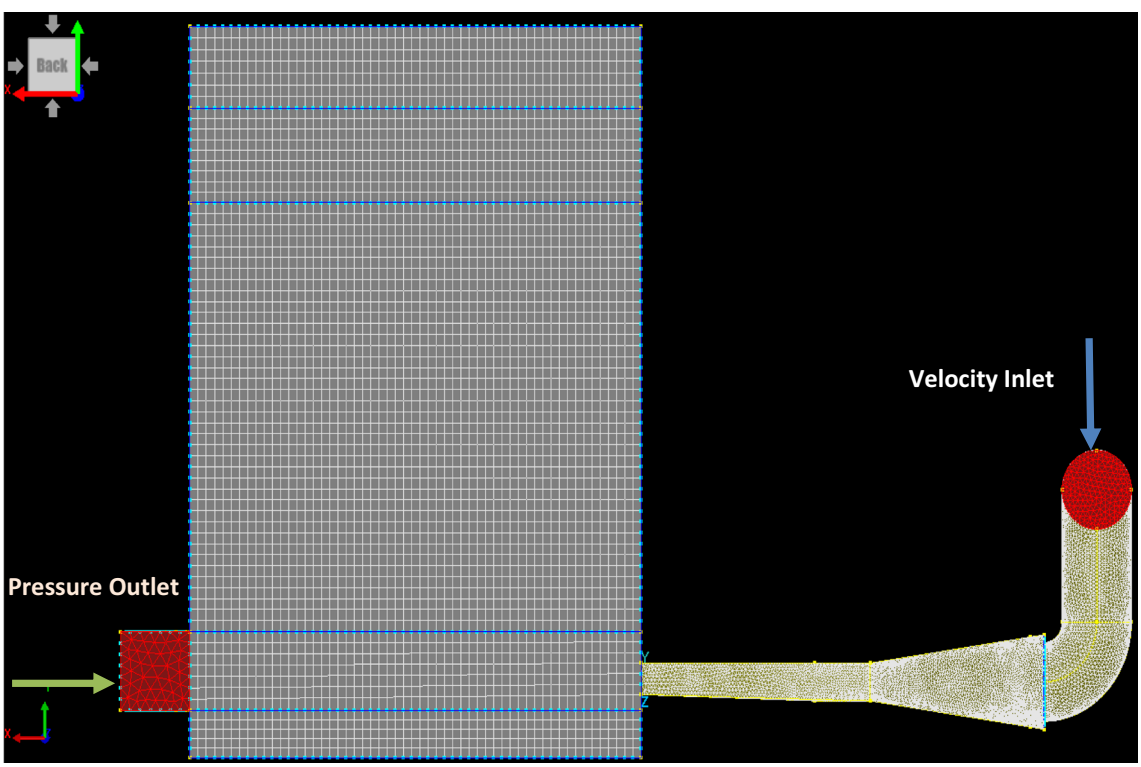

Fig. 6 The boundary conditions of the meshes

2.4 Uncertainty analyses

The accuracies of measured cross-flow velocity are influenced by the alignment of the pitot tube and the calibration error of the pressure transducer. A statistical analysis scheme, named Student's t distribution [15], was employed to the uncertainty analysis of the experiment in this study. It is expressed as

$$t = \frac{\bar{x} - \mu}{\sigma / \sqrt{n}} \tag{1}$$

where μ is the expectation value and n is the random sample number. $\bar{x}$ is the mean value of the recorded data and can be defined as

$$\bar{x} = \frac{1}{n} \sum_{i=1}^{n} x_i \tag{2}$$

The standard deviation σ_x can be calculated through

$$\sigma_x = \sqrt{\frac{1}{n-1} \sum_{i=1}^{n} \left(x_i - \bar{x} \right)^2} \tag{3}$$

The uncertainty of the conditions in three directions $\Delta\bar{x}$ can be computed through

$$\Delta \overline{X} = t_{n-1} \frac{\sigma_X}{\sqrt{n}} \tag{4}$$

where t_{n-1} that represents that the t distribution was $n - 1$ degree of freedom. The larger the degree of freedom, the closer to the normal density the t density will be. As the significant level of accuracy was considered as 95% confidence level, t_{n-1} approaches to 1.96. In this study, the uncertainty can be computed to be less than 3% with numbers of samples of 16,384.

3 Computational method

3.1 Methodology

The commercial software CFD-ACE+ (version 2015.0.0.11788) was used for the simulation in this study. To solve the steady-state Navier-Stokes equation, the first-order upwind scheme and SIMPLEC (Semi-Implicit Method for Pressure-Linked Equations Consistent) algorithm were applied. The second-order upwind scheme was employed for all the equations except transient formulation. It is accurate in space and time but introduces severe numerical diffusion/dissipation to the solution where large gradients exist. For the purpose of better predicting the free shear layer flow with small pressure gradients and wall-bounded flows, the standard and renormalization group (RNG) k-epsilon models were first selected as the turbulence models. The results showed that the RNG k-epsilon model failed to integrate the wall functions. The simulation results for the blow-to-suction system were verified through a comparison of the experimental results. Each computation consists of 2000 iterations. Convergence with a residual level of 10^{-4} is normally reached after approximately 1000 computations.

3.2 Grid and boundary condition

Table 1 presents the computational settings used in this simulation. Three-dimensional grids were generated for this blow-to-suction device. The origin of coordinate was set at the mid-section of the trapezoid push nozzle. The CFD-GEOM (version 2015.0.0.25) was used to generate the grid system. The domain of the blow-to-suction device was divided into three parts, the blowing device, the working chamber, and the suction tunnel. As shown in Fig. 4, the length, width, and height of the working chamber domain were set as 685, 325, and 464 mm, respectively. It is composed of 1,751,040 structured grids. The model of the trapezoid push nozzle is consisted of five baffles, the flow field development area, a straight round pipe with 50 mm diameter, and the bended side. The length of the suction tunnel is 490 mm, and a 50 mm × 50 mm square is specified as the outlet. As shown in Figs. 5 and 6, the push nozzle and suction tunnel were meshed using the unstructured grids, while the working chamber was constructed using structured grids. The interfaces in-between push nozzle/suction tunnel and working chamber are meshed using a hybrid mesh composed of structured and unstructured grids. In order to simulate the detail flow field of the blow-to-suction region, 25 layers of structured grid with the growing rate of 1.1 were generated all over the area to calculate the boundary layer flow and the location of vortex formation. Triangle cell type (AFM) with a max cell size of 8 and a min cell size of 1 was used. Conditions for simulation were chosen to be identical to the real case, including inlet Reynolds number (24,635), outlet pressure (101,300 Pa), temperature (300 K), and turbulence intensity (0.045%). The direction of the flow was specified in Cartesian coordinates. The degree of uniformity (DOU) was applied to confirm the quality of the flow, which can be expressed as

$$\mathrm{DOU} = \left(1 - \left(\frac{\Delta\bar{x}}{\bar{x}} \right) \right) \tag{5}$$

Table 2 Grid independency of surface grids with the DOU

Surface grids	DOU (%)
300 × 50	73.6
300 × 75	74.2
300 × 100	74.9
300 × 150	78.3
Experiment	75.2

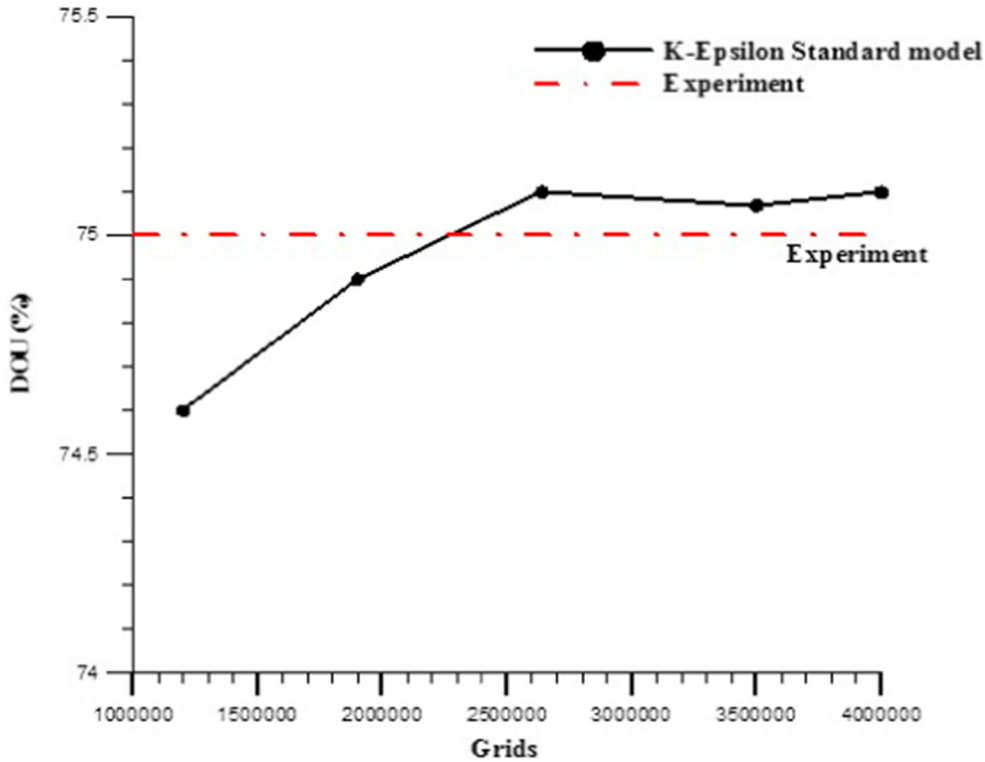

Fig. 7 Grid independency of overall grids with the DOU

3.3 Grid convergence study

The grid dependency was verified using different surface grid refinements for the boundary layer and domain. Smaller grids result in more accurate simulation; however, a longer computational time is expected. The surface grids, including upper and lower surfaces of the working chamber, of 300 × 150, 300 × 100, 300 × 75, and 300 × 50 were examined, as shown

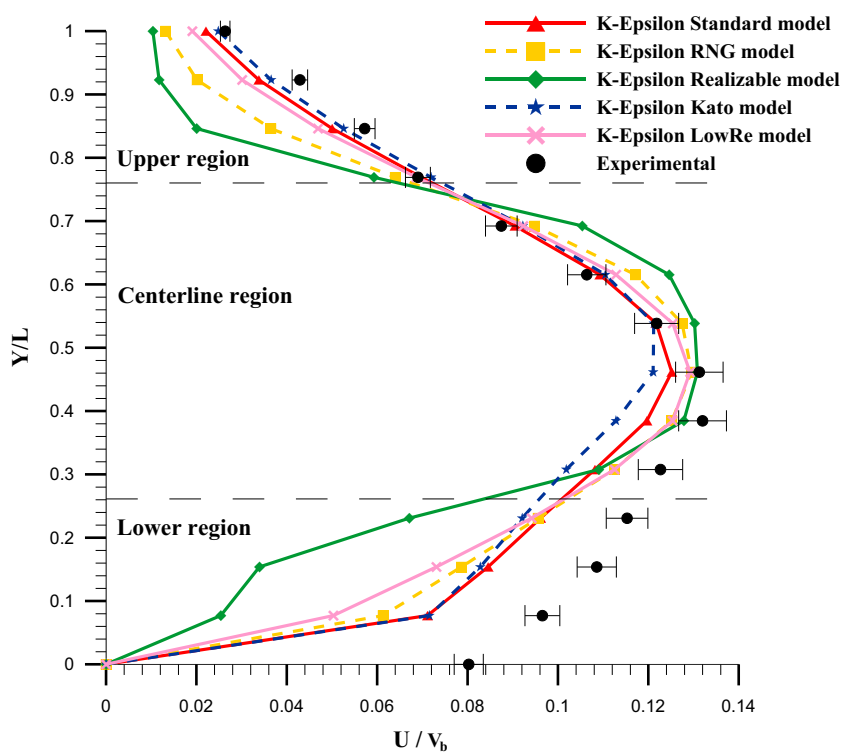

Fig. 8 The comparison of various turbulence models with experimental data for the centerline velocity distributions at V_b = 7 m/s and V_p = 13 m/s

in Table 2. It is clear that 300 × 100 is sufficient for convergence. In addition, overall grids of 1,200,000, 1,900,000, 2,600,000, and 3,500,000 were also tested for the grid convergence study. As shown in Fig. 7, it can be seen that the predicted DOUs increased with increasing overall grids and were stabilized after the overall grids reach 2,600,000. Therefore, the overall grids of 2,600,000 were chosen for the computation.

4 Results and discussion

4.1 Sectional velocity distributions

The experimental and simulated sectional velocity profiles are shown in Fig. 8. The values in *y*-axis represent the measuring distance from the bottom of the working chamber, which was divided into three regions: centerline region (between

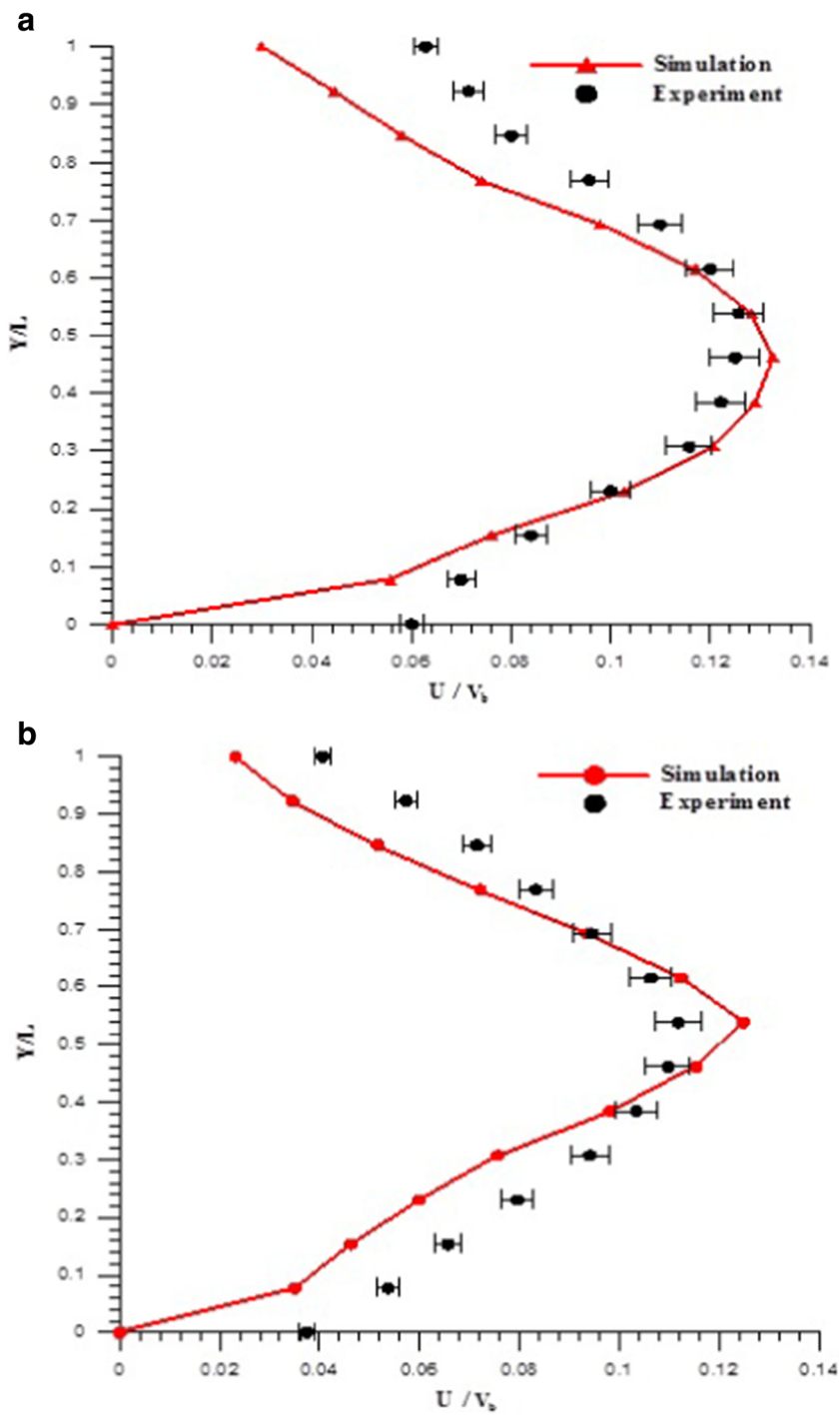

Fig. 9 The comparison of simulation and experimental velocity profiles for the cases of **a** 5–3 vs 5–3 and **b** 3–3 vs 5–3 (V_b = 7 m/s and V_p = 13 m/s)

$Y = 0.07$ m and $Y = 0.03$ m), upper region ($Y > 0.07$ m), and lower region ($Y < 0.03$ m). Relatively higher velocities were observed in the centerline region than in the upper and lower regions. The error bars of the experimental results represent the standard deviation of the measuring data. Five turbulence models, standard k-epsilon, RNG k-epsilon, realizable k-epsilon, Kato k-epsilon, and low Re k-epsilon, were examined, compared, and verified with the experimental data, for the purpose of examining the simulation accuracy. The experimental and simulated velocity profiles agree well, especially in the centerline region. Slight deviations between these two results were found at the upper and lower regions. The former was due to the intrusion of the hot-wire support, which accelerates the flow at the upper level of the working chamber. The latter comes from the incapability of velocity measurement near the ground of the working chamber. As seen in Fig. 8, the standard k-epsilon model demonstrated the best prediction for the experimental behavior; therefore, it is chosen as the turbulence model in the simulation.

4.1.1 Push nozzle width

The width of the trapezoid push nozzle (N) is one of the primary parameters that influences the flow uniformity of the working chamber. Figure 9a, b shows the experimental and simulation results obtained from the cases: $N = 3$ and 5 cm, S (suction tunnel width) = 5 cm, and H (nozzle-to-plane distances) = 3 cm (denoted as N–H vs S–H; 3–3 vs 5–3 and 5–3 vs 5–3). The push-nozzle velocity (V_b) and suction flow velocity (V_p) are 7 and 13 m/s, respectively. Deviations between simulation and experimental results occurred in the upper and lower regions for these two cases. For the upper region, the predicted velocities were an average of 23.8 and 18.9% lower than the experimental ones for the cases of 5–3 vs 5–3 and 3–3 vs 5–3, respectively, due to the placement of the hot-wire support. The average 23.1 and 17% differences between experimental and simulation data were found in the lower region, and the difference is reduced as Y/L is increased.

Figure 10 demonstrates the simulated velocity profiles for various push nozzle widths. The highest velocities were found along the centerline region, and they increased by 12~13.2% when the push nozzle width was enlarged from 2 to 5 cm. As the push nozzle width was reduced, i.e., cases of 2–3 vs 5–3 and 3–3 vs 5–3, it can be seen that the velocity profiles in the center region are sharper. It is noted that these velocity profiles were measured at the middle of the working chamber. Relatively high flow velocities were expected near the outlet of the nozzle due to a small cross-sectional area, causing significant energy loss and resulting in low velocities when the flow reaches the middle of the working chamber. The cases of 4–3 vs 5–3 and 5–3 vs 5–3 are more favorable because they represent more stable flow fields. The case of 4–3 vs 5–3 is better compared to the case of 5–3 vs 5–3 due to the enhanced velocity profile. For the purpose of preventing the metal powder from disturbing in a SLM chamber, a high velocity profile is preferred.

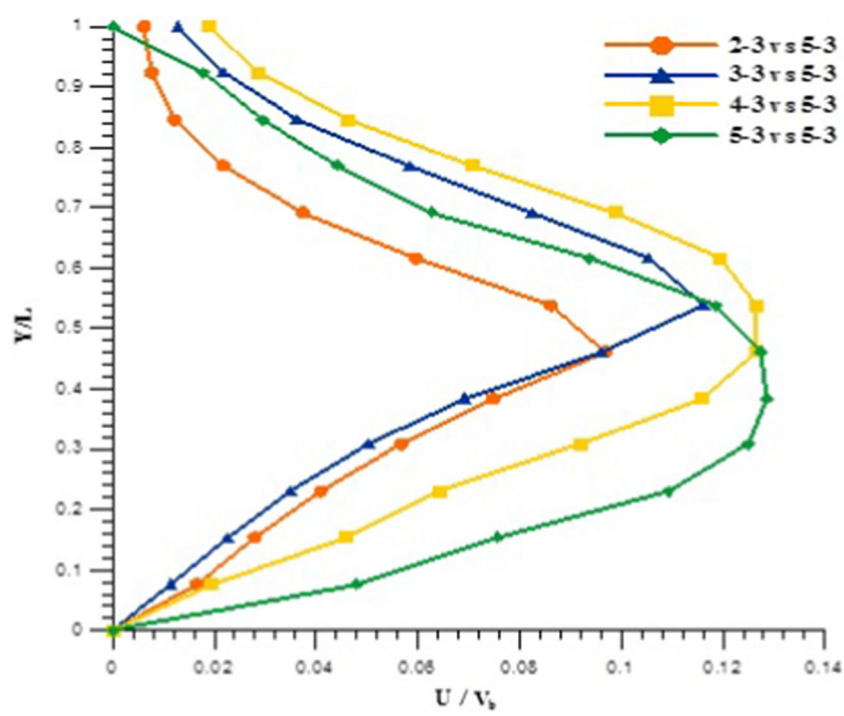

Fig. 10 The sectional velocity distributions for various push nozzle widths (V_b = 7 m/s and V_p = 13 m/s)

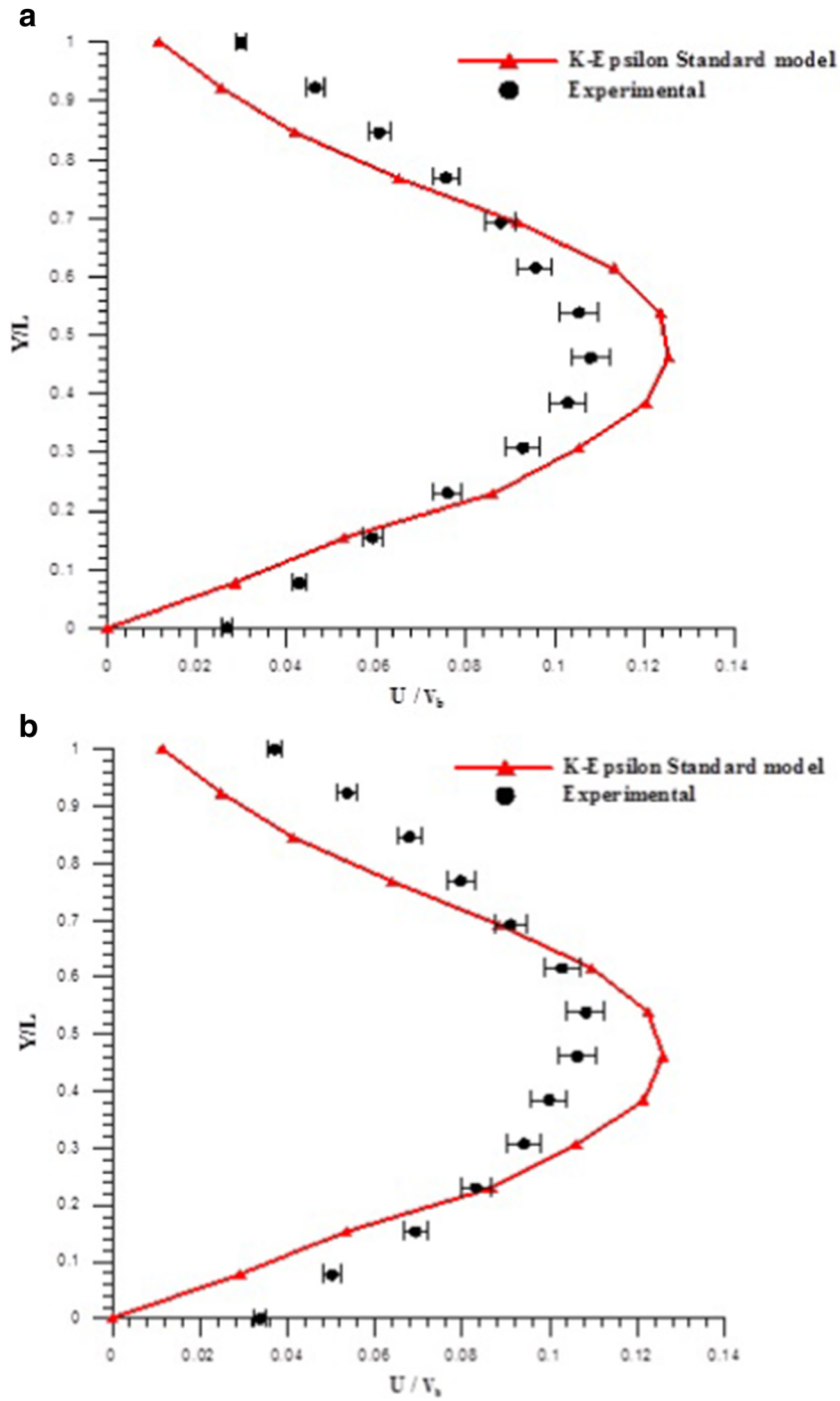

Fig. 11 The comparison of simulation and experimental velocity profiles for the cases of **a** 4–3 vs 4–3 and **b** 4–3 vs 3–3

4.1.2 Suction tunnel width

Figure 11 shows the comparison of simulated and experimental results for the two cases with different suction tunnel widths (4–3 vs 4–3 and 4–3 vs 3–3). It can be seen that velocities in the centerline region were slightly over-predicted by 9.3%. This is because the hot-wire probe for measuring the flow velocity was located in front of the suction tunnel, and the flow was decelerated by the wake of the probe.

Figure 12 shows the velocity profiles at various suction tunnel widths, ranging from 2 to 5 mm. Velocity profiles for these four cases are similar at the upper and center regions. Compared the case of 4–3 vs 2–3 to 4–3 vs 5–3, higher velocities were found for 4–3 vs 2–3 at the lower region. According to previous literatures, high suction velocity at the cross-

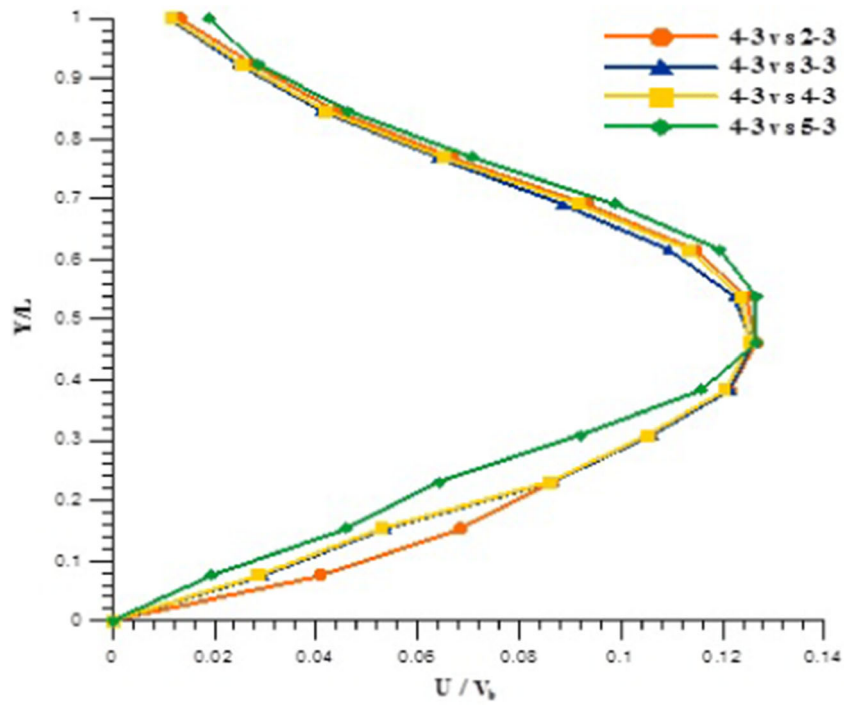

Fig. 12 The sectional velocity distributions for the various suction tunnel widths (V_b = 7 m/s and V_p = 13 m/s)

sectional area of suction tunnel favors the air-curtain flow inside the working chamber. Therefore, the case of 4–3 vs 2–3 is chosen as the optimal one among these four cases.

4.1.3 The nozzle-to-plane distances

Figure 13 shows the experimental and simulation results with varying nozzle-to-plane distances. An agreement was found between experimental and simulation data. A variation of the nozzle-to-plane distances, including 4–2 vs 2–2, 4–3 vs 2–3, 4–4 vs 2–4, and 4–5 vs 2–5, was examined and compared, as shown in Fig. 14. When the nozzle-to-plane distance increases, the velocity profile at the centerline region was lifted up. As mentioned in Section 4.1.1, enhanced velocity profile is favored for the SLM process. Reducing the nozzle-to-plane distance causes flow to touch the ground level more quickly, resulting in higher momentum loss.

4.2 Flow visualization

4.2.1 Flow patterns with different suction velocities at the beginning section

The flow patterns at the timeframe of 1.5 s were imaged through the laser-light sheet flow visualization technique, as shown in Fig. 15. Four Reynolds numbers with varying suction velocities were tested with fixed push nozzle velocity (7 m/s). As shown in Fig. 15a, vortices were formed above the streamwise flow at x/L = 0.525. As the suction velocity increases, which the Reynolds numbers were increased to 1.2×10^5, 2.16×10^5, and 3.12×10^5 (Fig. 15b–d), the vortices moved to x/L = 0.56, 0.6, and 0.7, respectively. It is believed that the vena contracta effect contributes the movement of vortices, resulting in the energy storage for the vortex formation [16]. It can also be seen that the vortex dissipation prevents the flow from moving downward to the working plane. The momentum was transported effectively so that the flow pattern can be attracted to the suction part continuously.

4.2.2 Flow patterns with different suction velocities at the contacting section

Four types of flow patterns as t = 3 s were also imaged, as shown in Fig. 16. As seen in Fig. 16a–d, the jet flow emitted from the push nozzle starts reaching the working plane at the locations of x/L = 0.43, 0.48, 0.73, and 0.81, respectively. Practically, the push nozzle velocity and the width of the working chamber have to be constrained due to the industrial laminated manufacturing system (LMS) design regulation. The flow pattern tended to drop down due to the Coanda effect. As the suction velocity increased, the *touch-down* locations move toward the suction tunnel, which is beneficial to the SLM process. It can also be seen that the vertical structures are more organized as higher suction velocity was applied. Lower suction velocity resulted in a less momentum exchange

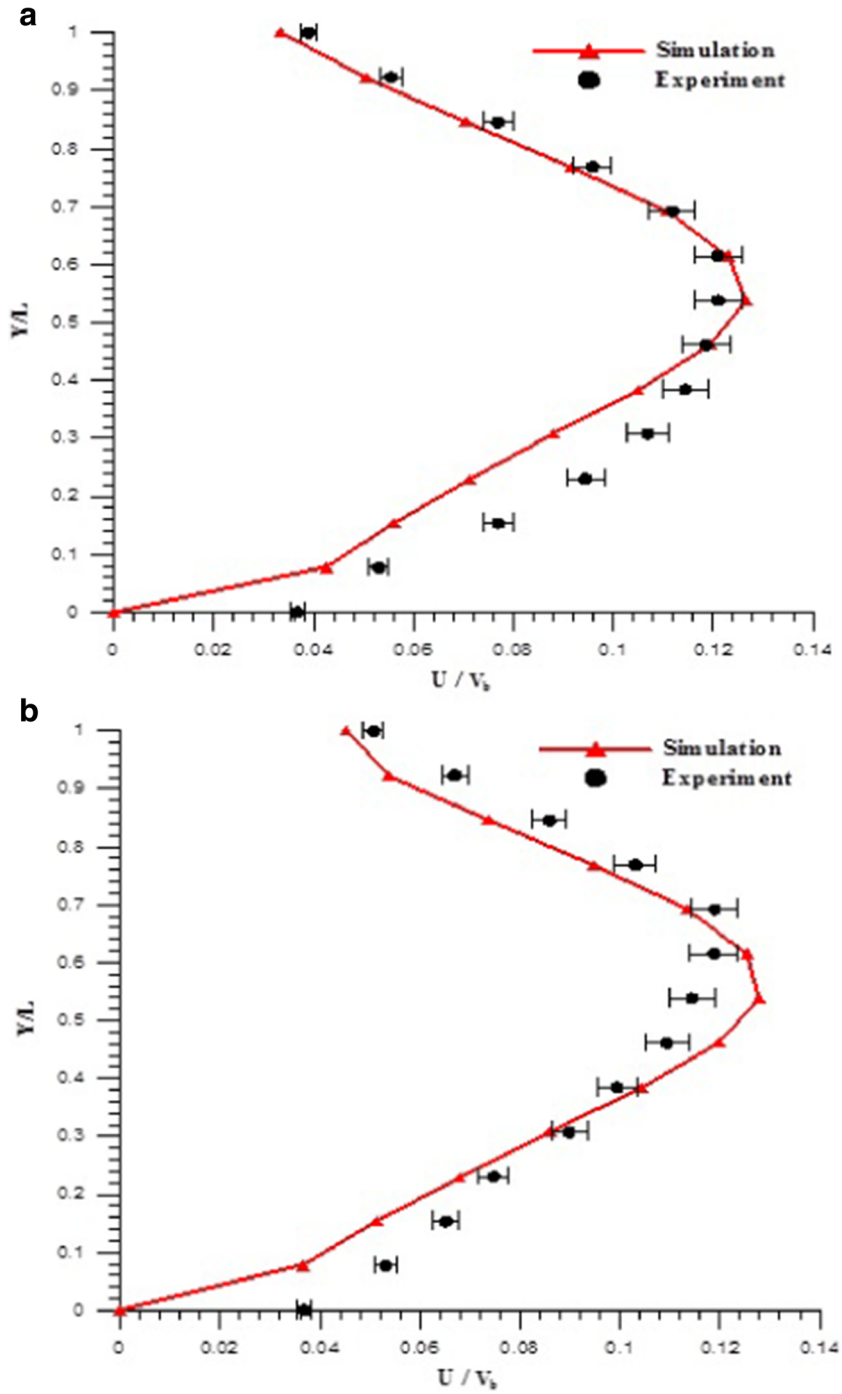

Fig. 13 The comparison of simulation and experimental velocity profiles for the cases of **a** 4–4 vs 2–4 and **b** 4–5 vs 2–5

in-between blow and suction sides, leading to higher shear effect and vortex rollup along the jet boundary. High suction velocity delays the vortex forming and reduces the energy dissipation, resulting in a uniform flow pattern in the working chamber. The instantaneous images for the flow patterns at the Reynolds number of 3.12×10^5 are shown in Fig. 17. It can be observed that the vortex starts forming at $t = 1.4$ s (plot 2) and becomes more organized at $t = 1.8$ s (plot 3). The phenomena of the first vortex merging and rollup were found at $t = 1.8$ s (plot 3). Additionally, it appears that the flow pattern starts moving downward at $t = 1.8$ s (plot 3) due to the energy dissipation. The second vortex merging was found at $t = 2.2$ s (plot 4), which resulted in a larger vertical structure. At further downstream, it is interesting to find the occurrence of flow entrainment at $t = 2.2$ s (plot 4) and $t = 2.6$ s (plot 5). However,

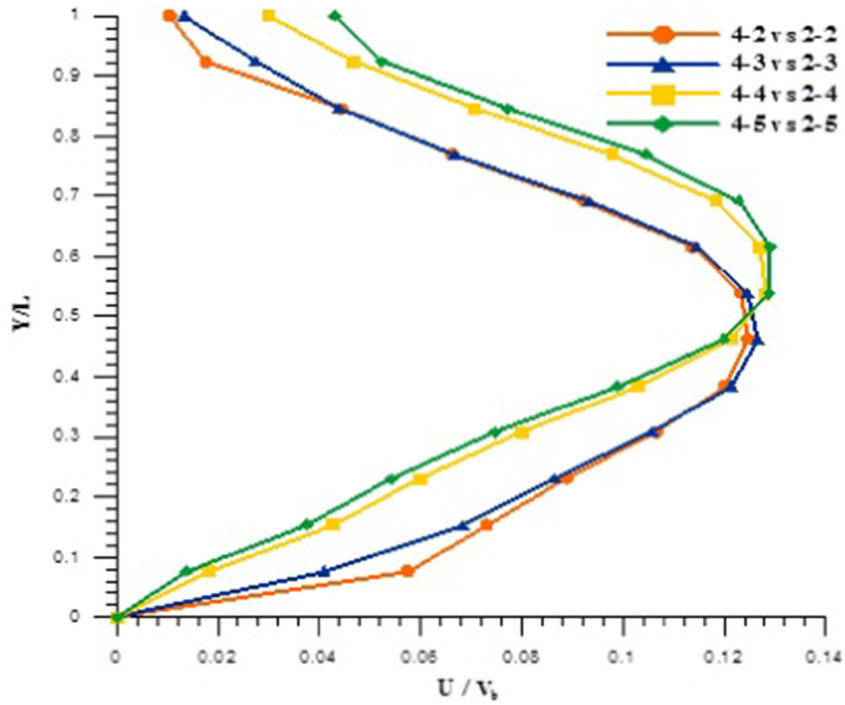

Fig. 14 The sectional velocity distributions for various nozzle-to-plane distances (V_b = 7 m/s and V_p = 13 m/s)

high suction velocity overcomes the flow entrainment and attracts the flow pattern to the suction side. At t = 3 s (plot 6), the flow pattern was raised and absorbed into the suction tunnel.

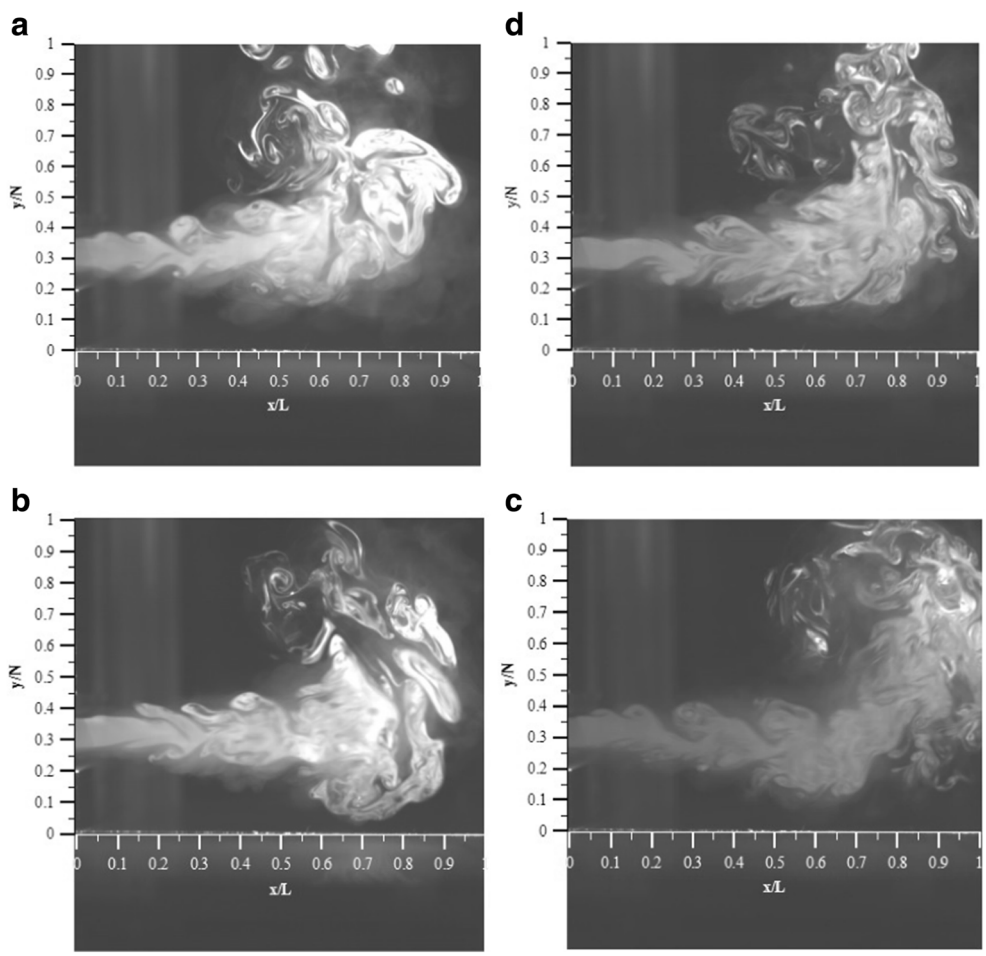

Fig. 15 Smoke visualization images at **a** Re_L of 2.4×10^4, **b** Re_L of 1.2×10^5, **c** 2.16×10^5, and **d** Re_L of 3.12×10^5 (t = 1.5 s)

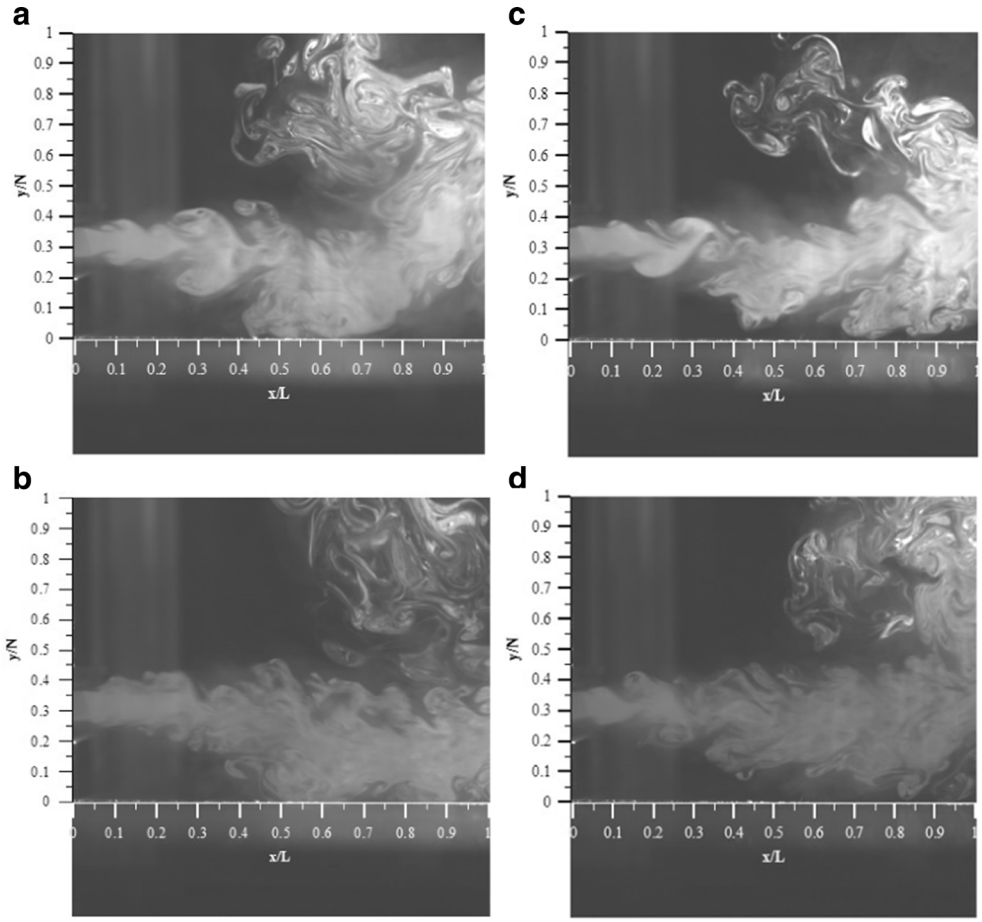

Fig. 16 **a** Smoke visualization image for the Re_L of 2.4×10^4 at $t = 3$ s. **b** Smoke visualization image for the Re_L of 1.2×10^5 at $t = 3$ s. **c** Smoke visualization image for the Re_L of 2.16×10^5 at $t = 3$ s. **d** Smoke visualization image for the Re_L of 3.12×10^5 at $t = 3$ s

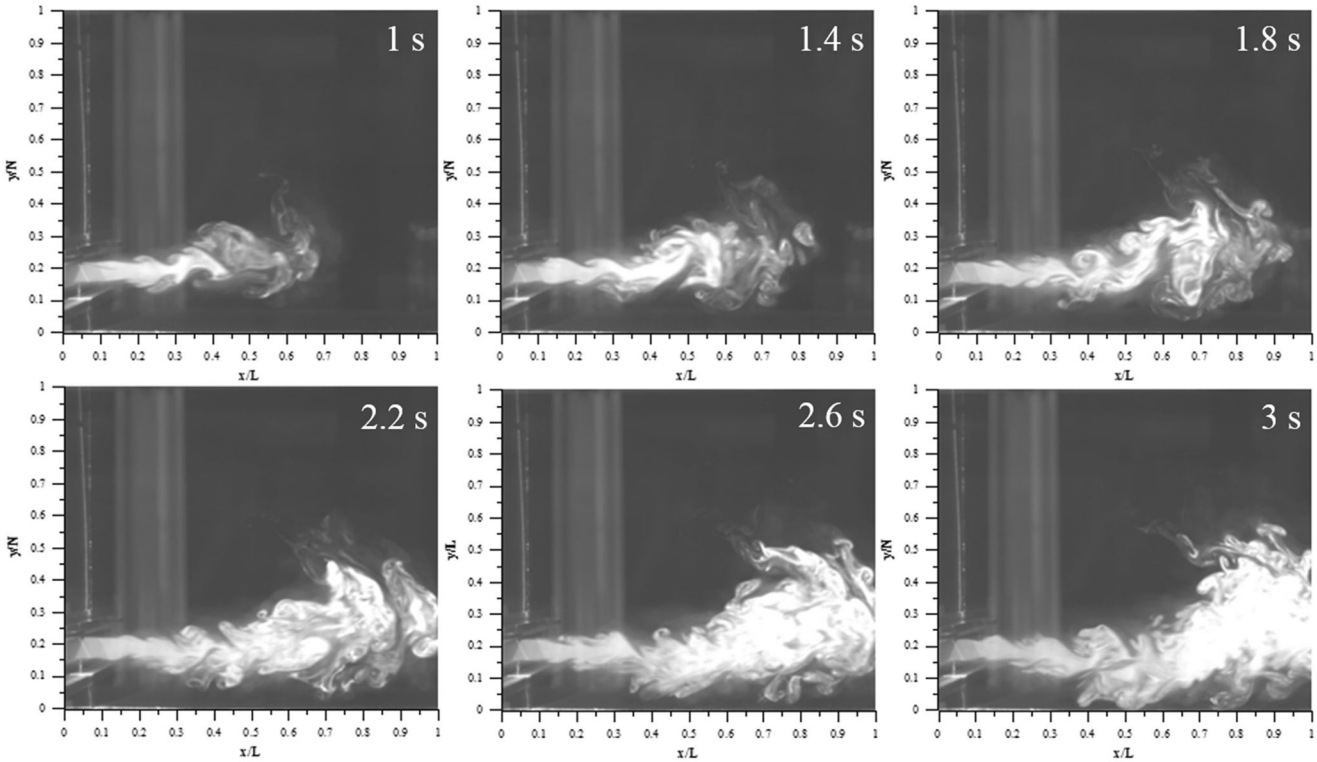

Fig. 17 Instantaneous flow images of coherent structure evolution at $Re_L = 3.12 \times 10^5$ at $t = 1$~3 s

Table 3 The DOUs at various parameters (*N–H* vs *S–H*)

	Experimental (%)	Simulation (%)	Error (%)
Push nozzle width			
5–3 vs 5–3	86.7	81.3	15.8
4–3 vs 5–3	90.6	84.1	16.8
3–3 vs 5–3	83.1	78.6	15.2
2–3 vs 5–3	79.2	74.7	15.1
Suction tunnel width			
4–3 vs 4–3	79.6	74.3	8.7
4–3 vs 3–3	82.6	75.8	10.9
4–3 vs 2–3	85.7	78.4	11.5
Nozzle-to-plane distance			
4–5 vs 2–5	83.1	79.2	9.3
4–4 vs 2–4	81.4	78.4	8.1
4–2 vs 2–2	77.8	77.5	5.9

4.3 The degree of uniformity

Table 3 shows the DOUs at various parameters obtained from experiment and simulation. Errors between the experimental and simulating DOUs were within 5.9 and 16.8%, which is in an acceptable range. It appears that a short push nozzle width results in the low DOU. With the same blowing velocity, shorter push nozzle width leads to higher flow velocity inside the chamber, causing a higher instability of the flow field and lower uniformity of the flow. It can be seen that more than 90% of DOUs was obtained in the case of 4–3 vs 5–3. As varying the suction tunnel width, it was observed that a short suction tunnel width leads to a high DOU. Almost 86% of uniformity was found experimentally in the case of 4–3 vs 2–3. When decreasing the suction tunnel width, the flow accelerates at the interface of the suction side, resulting in a higher momentum exchange between the push nozzle and suction tunnel, which causes a higher uniformity of the flow. As expected, a large nozzle-to-plane distance leads to a high DOU. Around 83% was obtained in the case of 4–5 vs 2–5. Among all the parameters, the case of 4–3 vs 5–3 was selected to be the optimal case with the highest DOU, which is expected to absorb the used metal powders to the suction side successfully in the LMS chamber.

4.4 The simulation of metal powder removal

The particles with an identical size of 50 μm and a density of 8000 kg/L were chosen to simulate the metal powders inside the working chamber with the optimal design of the LMS, as shown in Fig. 18. The initial ejecting velocity of the particle was set to be 2 m/s in the *y*-direction, and the initial locations of the particles were distributed along Z = 75, 25, −25, and −75 mm and Y = −32 mm. The time step size of 0.02 and the time step number of 100 were applied in the simulation. It can be seen from the results that the particles were ejected with a parabolic shape to 45 mm from the bottom of the working chamber, dropped down to 25 mm from that, and successfully been carried away into the suction tunnel because of the high uniformity of the flow.

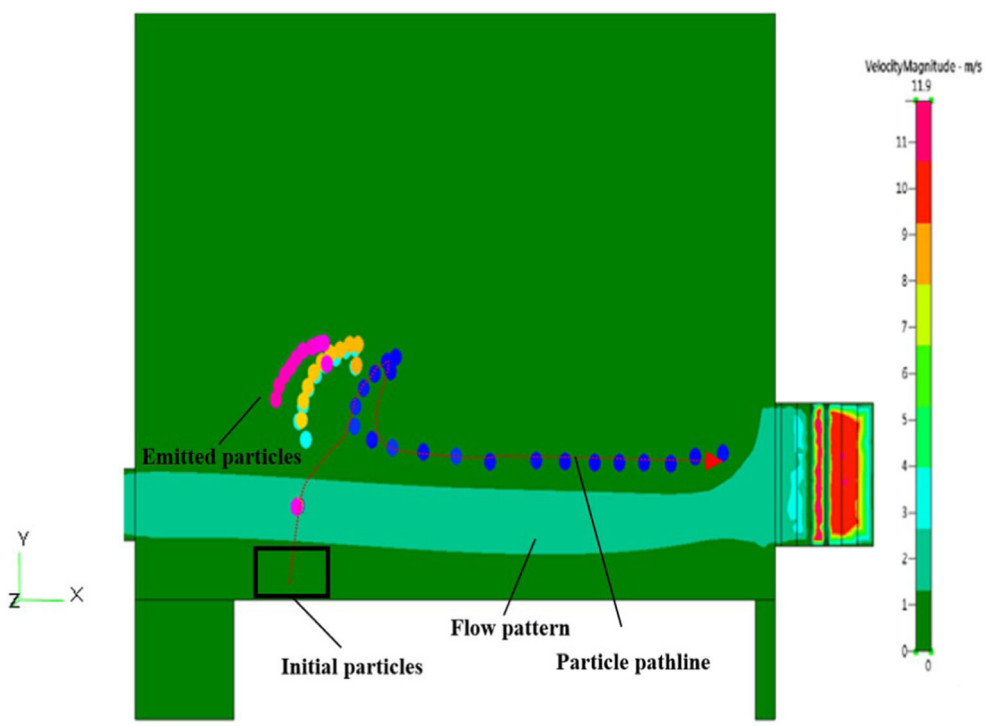

Fig. 18 The path lines of the metal powder at the different locations of the working chamber

5 Conclusions

In this study, for the purpose of improving the DOU across the SLM working chamber, the flow characteristics with varying trapezoid push nozzle widths, suction tunnel widths, and nozzle-to-plane distances in a blow-to-suction device were investigated experimentally and computationally. Based on the results of velocity profile, flow visualization, and DOU, the following conclusions were specified:

1. Decreasing the width of the trapezoid push nozzle, with the same blowing velocity, results in a relatively high instability of the flow field and decreases the flow uniformity.
2. Decreasing the width of the suction tunnel leads to a better momentum exchange between the blowing and suction sides. This maintains the uniformity of the flow inside the working chamber. In addition, this enhances the velocity profile of the flow and prevents the flow from disturbing the on-site metal powders.
3. Increasing the nozzle-to-plane distance results in the enhanced velocity profile and helps the absorption of the flow to the suction side.
4. The delay of vortex forming was found at high suction velocities. Energy dissipation can therefore be avoided, and the flow uniformity can be maintained.
5. A higher momentum exchange employed in-between the blow and suction sides reduces the energy loss as the flow passing through the working chamber, thereby resulting in better flow uniformity.

Acknowledgments This work was supported by the Ministry of Economic Affairs, Taiwan, through the Grant "A+ Industrial Innovative and Research Project-Advanced Technology Research."

References

1. Ferrar B, Mullen L, Jones E, Stamp R, Sutcliffe CJ (2012) Gas flow effects on selective laser melting (SLM) manufacturing performance. J Mater Process Technol 212:355–364
2. Dai D, Gu D (2014) Thermal behavior and densification mechanism during selective laser melting of copper matrix composites: simulation and experiments. Mater Des 55:482–491
3. Marzal F, González E, Miñana A, Baeza A (2002) Analytical model for evaluating lateral capture efficiencies in surface treatment tanks. AIHA J 63:572–577
4. Marzal F (2002) Influence of push element geometry on the capture efficiency of push-pull ventilation systems in surface treatment tanks. Ann Occup Hyg 46:383–393
5. Marzal F, González E, Miñana A, Baeza A (2003a) Visualization of airflows in push-pull ventilation systems applied to surface treatment tanks. AIHA J 64:455–460
6. Marzal F, González E, Miñana A, Baeza A (2003b) Methodologies for determining capture efficiencies in surface treatment tanks. AIHA J 64:604–608
7. Tseng L-C, Huang RF, Chen C-C, Chang CP (2006) Correlation between airflow patterns and performance of a laboratory fume hood. J Occup Environ Hyg 3:694–706
8. Chen J-K, Huang RF, Hsin P-Y, Hsu CM, CHen C-W (2012a) Flow and containment characteristics of an air-curtain fume hood operated at high temperatures. Ind Health 50:103–114
9. Jia-Kun C, Huang RF (2014) Flow characteristics and robustness of an inclined quad-vortex range hood. Ind Health 52:248
10. Chen JK, Huang RF, Hsin PY (2012b) Dynamic effects on containment of air-curtain fume hood operated with heat source. J Occup Environ Hyg 9:640–652
11. Chen JK, Huang RF, Hung WL (2013) Flow and leakage characteristics of a sashless inclined air-curtain (sIAC) fume hood containing tall pollutant-generation tanks. J Occup Environ Hyg 10:694–704
12. Huang RF, Chen JK, Han MJ, Priyambodo Y (2014) Improving flow patterns and spillage characteristics of a box-type commercial kitchen hood. J Occup Environ Hyg 11:238–248
13. Huang RF, Chen JK, Hung WL (2013) Flow and containment characteristics of a sash-less, variable-height inclined air-curtain fume hood. The Annals of Occupational Hygiene 57:934–952
14. Huang RF, Lin SY, Jan SY, Hsieh RH, Chen YK, Chen CW et al (2005) Aerodynamic characteristics and design guidelines of push-pull ventilation systems. The Annals of Occupational Hygiene 49:1–15
15. Bendat JS, Piersol AG (2011) Random data: analysis and measurement procedures. John Wiley & Sons, Hoboken
16. Hsiao F-B, Lim Y-C, Huang J-M (2010) On the near-field flow structure and mode behaviors for the right-angle and sharp-edged orifice plane jet. Exp Thermal Fluid Sci 34:1282–1289